Photovoltaic and photocatalytic performance of electrospun Zn_2SnO_4 hollow fibers

Partha Pratim Das [a,c,1], Anurag Roy [a,c,1], Mukta Tathavadekar [b,c], P. Sujatha Devi [a,c,*]

[a] Sensor and Actuator Division, CSIR-Central Glass and Ceramic Research Institute, Kolkata 700032, India
[b] Physical and Materials Chemistry Division, CSIR-National Chemical Laboratory, Pune 411 008, India
[c] CSIR- Network Institute of Solar Energy (CSIR-NISE), New Delhi, India

ARTICLE INFO

ABSTRACT

The phase pure hollow Zn_2SnO_4 and green emitting ZnO-SnO_2-Zn_2SnO_4 composite fiber have been prepared by post calcining the as formed fiber by electrospin technique. Depending upon the calcination temperature, the as prepared fiber exhibited a striking variation in composition, microstructure, optical and photo-electrochemical properties. The composition dependent dissimilarity in photovoltaic performance and photocatalytic activity has been established in this work. A relatively enhanced open circuit voltage (Voc) of 0.76 V, fill factor (FF) of 59.78%, short circuit current (Jsc) of 4.2 mA/cm^2 and an overall conversion efficiency (η) of 1.93% have been achieved for the phase pure Zn_2SnO_4 porous fiber obtained at the elevated calcination temperature of 1000 °C. On the contrary, a relatively reduced Voc, FF, J_{SC} and η of 0.70 V, 42.54%, 3.8 mA/cm^2 and 1.17%, respectively, have been achieved for the 800 °C calcined dense fiber consisting of a mixture of three distinct phases ZnO, SnO_2 and Zn_2SnO_4. Unlike photovoltaic behaviour the trend in photocatalytic performance interestingly got reversed for the ZnO-SnO_2-Zn_2SnO_4 composite fiber owing to its superior photo-induced charge separation ability followed by generation of larger amount of active hydroxyl radicals (OH·). Our results establish the composite fiber as a preferred photocatalyst in comparison to phase pure Zn_2SnO_4 towards the textile dyes Methylene blue and Congo red and non absorbing organic pollutants such as Phenol and Bisphenol A under UV illumination.

© 2016 Elsevier B.V. All rights reserved.

1. Introduction

One dimensional (1D) semiconducting oxides of various morphologies such as rods, wires, tubes, belts, fibers etc. are exceptionally impressive towards diverse applications [1–10]. For instance, the emerging photovoltaic device dye sensitized solar cells (DSSCs) and the green approach of removing toxic waste water pollutant through photocatalysis are noteworthy. The metal oxide fiber has been exploited to a lesser extent as the photoanode-photocatalyst materials in the above mentioned areas compared to other 1D morphologies where 1D fibers with controllable length to diameter ratio, porous fibers, hollow fibers, cable like multi-core fibers and so forth could be effective enough for the same [11–16]. In this regard, the composition of the materials also plays a significant role along with the morphology. Apart from the mostly studied simple binary oxides such as TiO_2, ZnO, SnO_2, Nb_2O_5, In_2O_3,

Bi_2O_3 and Fe_2O_3 the ternary oxides by coupling of metal oxides or the semiconductor–semiconductor heterojuction are of equally fascinating owing to their modified electronic and optical properties [17–19]. Interesting reports are also available on various Bi based ternary oxides and hypohalides exhibiting quite appreciable inorganic-organic pollutant removal capabilities [20–24]. The performances of these ternary oxide based systems regarding photodegradation of waste water pollutant turned out more impressive upon modifying with quantum dots, p-type materials, metal ion doping etc. where the possibility of photo-induced charge separation has been reported to suppress the recombination reaction. For example, Bi_2WO_6 modified with carbon quantum dot has been introduced for the removal of gaseous volatile organic compounds (VOC) [20]. Liang et. al., elsewhere reported the Ag treated Bi_2WO_6 and its enhanced photocatalytic activity towards RhB dye [21]. $BiPO_4$ has also been claimed to be effective for organic contaminanta degradation with the help of p-type Cu_2O nanoparticles [22]. In addition, Cui et. al., highlighted Cu_2O quantum dot embedded flower-like BiOBr for enhanced photocatalytic activity [23]. Zhua et. al., reported MB degradation with improved photocatalytic performance by $BiPO_4$/Bi_2WO_6 dual ternary oxides composite [24]. Other than hazardous Bi, Ag based semiconducting oxides for instance

* Corresponding author at: Sensor and Actuator Division, CSIR-Central Glass and Ceramic Research Institute, Kolkata 700032, India.
E-mail addresses: psujathadevi@cgcri.res.in, psujathadevi@gmail.com (P.S. Devi).
[1] ¹Both the authors contributed equally

Ag_3PO_4 has also been reported to be effective for the same [25]. Reports on Ag modified $K_4Nb_6O_{17}$, another interesting ternary oxide as an efficient photocatalyst owing to its plasmonic behavior is noteworthy [26]. Very recently, Wang et. al., reported the hydrothermally synthesized SnO_x/Zn_2SnO_4 composite having wide heterojunction separation of electrons and holes for improved photocatalytic activity [27]. Taking into account all the feasibilities, it could be interesting to study the performance of the ternary oxide Zn_2SnO_4 having high electron mobility ($10–15\,cm^2\,V^{-1}s^{-1}$), high electrical conductivity ($\sim10^4\,S\,cm^{-1}$), sufficient thermodynamic stability and fascinating optical properties with typical fiber morphology in photovoltaic and photocatalytic application [28,29]. In addition, the approach in utilising the $ZnO-SnO_2-Zn_2SnO_4$ composite oxide fiber having a combination of the unique features of both the binary and ternary oxides is also significant. Among some common synthetic methods such as chemical vapour deposition, hydrothermal and template assisted technique etc. the electrospun has been characterised to be an effective and versatile technique to fabricate the 1D fibers [11]. In this work, we have reported a successful preparation of dense and fluorescent $ZnO-SnO_2-Zn_2SnO_4$ composite fiber and phase pure Zn_2SnO_4 porous fiber by calcining the as prepared fiber at two different temperatures of 800 and 1000 °C respectively, where the as prepared fiber have been synthesized by the electrospin technique. The transformation of the green emitting binary-ternary oxide composite fiber to the phase pure hollow ternary oxide fiber as a function of temperature has been systematically monitored. The combined effect of the composition, microstructure and optical properties of the two distinct kinds of fibers on the DSSCs performances has been evaluated and thereafter compared their efficiency towards the degradation of textile dyes Methylene blue (MB) and Congo red (CR). Finally, the photocatalytic activities of the electrospun fiber samples were further verified for Phenol and Bisphenol A, as representative non-absorbing organic pollutants.

2. Experimental section

2.1. Preparation of fiber

Poly (methyl methacrylate) [PMMA, Mw = 350,000 mol/g], Zinc Acetate [$Zn(CH_3COO)_2 \cdot 2H_2O$, 99%] and Tin Acetate [$Sn(CH_3COO)_4$, 99%) Anhydrous N, N-dimethylformamide [ACS N,N-DMF, 99.8%] was obtained from Merck, India. All the chemical reagents had been used without further purification. The precursor solution has been prepared by dissolving 1.756 g of Zinc acetate, 1.42 g of Tin acetate and 1.5 g of PMMA simultaneously in 15.8 ml of DMF. The as prepared fiber was prepared by electrospinning the viscous precursor in a NaBond Electrospinning Unit, Standard Type. During the electrospinning process the solution was injected through a stainless steel needle (25 gauge, orifice diameter = 250 μM) which had been connected to a high-voltage DC power supply (Bertan, High-voltage power supply series 230). The solution was injected through a nozzle using a syringe pump (KD scientific, 781200) at an injection rate of 1.2 ml/h in a continuous fashion. The applied voltage was 17.25 KV between the needle and the rolling drum, located 15 cm below the needle. The dense $ZnO-SnO_2-Zn_2SnO_4$ composite fiber was obtained by calcining the as prepared fiber at 800 °C whereas pure Zn_2SnO_4 porous fiber has been formed by calcining the same at 1000 °C.

2.2. Material characterization

Thermo gravimetric analysis (TGA) and differential scanning calorimetric (DSC) studies of the as synthesized fiber was carried out from RT to 1200 °C with a heating rate of 10 °C/min on a NETZSCH 449C simultaneous thermal analyser to understand the thermal decomposition nature and temperature dependent phase formation. The calcined fibers have been characterised by powder X-ray diffraction (XRD) analysis on a X'pert pro MPD XRD of PAN analytical with Cu K_α radiation (λ=1.5406 A°) for identifying the phases formed. The morphology of the calcined samples was monitored through scanning electron microscope (SEM), (LEO 430i, Carl Zeiss) and high resolution transmission electron microscope operating at 300 kV (Tecnai G2 30ST, FEI). In order to verify the transformation of phases with increasing temperature fourier transform infrared (FTIR) absorption spectra of the samples were recorded on a Nicolet 380 FTIR spectrometer. For further confirmation, the Raman spectra were also obtained using a Renishaw InVia Reflex micro Raman spectrometer with excitation of argon ion (514 nm) lasers. The spectra were collected with a resolution of $1\,cm^{-1}$. X-ray photoelectron spectroscopy (XPS) measurements were carried out in a PHI 5000 Versa probe II scanning XPS microprobe (ULVAC-PHI, U.S.). The measurements were performed at room temperature and at a base pressure better than 6×10^{-10} mbar. All spectra were recorded with monochromatic Al Kα (hν = 1486.6 eV) radiations with a total resolution of about 0.7 eV and a beam size of 100 μm. The diffuse reflectance (DR) spectra of the composite and phase pure fibers have been measured using UV–vis-NIR spectrometer (Shimadzu UV-3600) to calculate the band gaps of the same. The optical properties of the fibers were evaluated by recording the room temperature emission spectrum on a steady state spectrofluorometer (QM-40, Photon Technology International, PTI) using a 150 W Xenon lamp as an excitation source. The fluorescence images of the fibers have been captured through a Nikon ECLIPSE TS100 inverted microscope utilising the same excitation source of the steady state spectrofluorometer unit. Nitrogen adsorption-desorption measurements were conducted at 77 K with a Quantachrome (iQ3,USA) instrument. The samples were outgassed in a vacuum at 150 °C for 2 h prior to the measurement. The surface area was obtained using the Brunauer-Emmet-Teller (BET) method within the relative pressure (p/p0) range of 0.05–0.20, and the pore size distribution was calculated by the Barret-Joyner-Halenda (BJH) method. The nitrogen adsorption volume at the relative pressure (p/p0) of 0.99 was used to determine the pore volume.

2.3. Adsorption ability of the sensitizer N719 and fabrication of the DSSC

Films with both the fibers were made by the doctor blade method on FTO glass (7 Ω/cm^2) and annealed at 450 °C for 1 h. The thickness of the films were maintained around 6–7 μm. A 0.5 mM solution of N719 dye in ethanol was used as the sensitizer and the dipping time was fixed for 12 h. In order to measure the dye adsorbing ability, the fabricated films were dipped in 0.5 mM N719 solution at room temperature. The concentrations of the residual dye solutions were measured by UV–vis absorption spectroscopy. The amount of dye adsorbed has been calculated by using the formula (C_0-C)/C_0, where C_0 is the initial concentration of the N719 dye and C is the percentage of residual dye in the solution [10]. The I–V characteristics were measured using a solar simulator (Newport) at 100 mW/cm^2 (1 Sun AM 1.5). Standard silicon solar cell (SER NO. 189/PVM351) from Newport, U.S. was used as a reference cell. The data presented are an average of measurements taken on three different devices for each sample.

2.4. Photocatalytic activity study

For a typical experiment, the photocatalytic activity of the fiber samples were evaluated by adding 100 mg of the fibers to the aqueous solutions of 10^{-5} (M) MB and CR separately. For the

degradation study of the phenolic compounds 10 ml of 3.7×10^{-3} (M) Phenol and Bisphenol A have been used. The solutions were stirred on a magnetic stirrer in dark for 30 min in order to achieve the adsorption-desorption equillibrium. An 8W UV lamp (UVLS-28 EL Series) having an average light intensity of $0.6 \, mW/cm^2$ and an emitting wavelength of 254 nm (UVC, 4.88 eV) was used as the irradiation source. The chronoamperometric studies (transient photocurrent responses) and electrochemical impedance spectra (EIS) (Nynquist plots) have been carried out by a Metrohm, Auto-lab AUT 85930 POTENTIOSTAT/GALVANOSTAT instrument with a standard three electrode cell where the photocatalyst, platinum wire, Ag/AgCl (3 M KCl) and 0.1 M K_2SO_4 were used as the working electrode, counter electrode, reference electrode and electrolyte, respectively, maintaining the same irradiation source used for pho-todegradation experiments. The chronoamperometric studies were performed at zero bias potential vs Ag/AgCl/3 M KCl while EIS were recorded in the frequency range of 0.1 Hz–100 KHz with 10 mV AC amplitude. The photodegradation profile was measured by moni-toring the change in the absorbance of MB and CR upon exposure to UV light in presence of the catalyst. The time-dependent absorption spectra of the dye solutions were measured on a UV–vis–NIR spec-trometer (Shimadzu UV-3600). The efficiency of degradation was calculated as $[(I_0-I)/I_0] \times 100$, where I_0 implies initial absorption intensity of MB and CR solution at 668 and 497 nm, respectively, and I represents absorption intensity of the same after degradation. C_0 is the initial concentration of the dye solutions whereas C indicates concentration of the dye solutions after photodegradation.

3. Results and discussion

The thermal decomposition nature of the as prepared fiber shown in Fig. 1 exhibited an overall weight loss of 60.56% within a temperature ranging of room temperature to 1000 °C. Three con-secutive weight loss steps terminating at around 200, 480 and 525 °C mainly represent the liberation of the adsorbed water, decomposition of excess acetate and formation of ZnO, SnO_2 and Zn_2SnO_4 in different proportions. Eventually, the weight loss became negligible beyond 700 °C. On the contrary, the DSC curve exhibited a sharp exotherm at around 490 °C with a small inflection around 375 °C. The depressed exotherm at around 950 °C interest-ingly indicates the formation of Zn_2SnO_4 from a formerly formed ZnO and SnO_2 mixture. Based on the TG-DSC analysis we have calcined the as prepared fiber in three different temperatures start-ing from 700 °C to an elevated temperature of 1000 °C whereas an intermediate temperature of 800 °C has also been fixed for the same. In order to ascertain the change in composition with calci-nation, a successive X-ray powder diffraction of the calcined fibers has been studied as exhibited in Fig. 2. The XRD pattern admit-tedly manifested the existence of all the three phases ZnO, SnO_2 and Zn_2SnO_4 in a slightly discrete proportion in the fiber calcined at 700 and 800 °C (Fig. 2c and d). For easier assimilation the diffrac-tion patterns of the composite powder, standard ZnO (JCPDS No: 36–1451) and SnO_2 (JCPDS No: 03-1114) have also been plotted, respectively, in Fig. 2a and b. It is worth mentioning the effective formation of the composite fiber as a phase pure spinel Zn_2SnO_4 (JCPDS No: 74–2184) upon calcination at 1000 °C (Fig. 2e). This con-firms the formation of both ZnO-SnO_2-Zn_2SnO_4 composite fiber and phase pure Zn_2SnO_4 fiber which are well crystalline indeed by this electro spinning technique. Microstructures of both the ZnO-SnO_2-Zn_2SnO_4 composite and phase pure Zn_2SnO_4 have been successfully verified by FESEM and TEM studies. In Fig. 3a–c FESEM images of the formed composite taken at various magnifications have been presented. Fig. 3a and b manifest a collection of ran-domly oriented fibers of different length. The magnified FESEM image of a single fiber in Fig. 3c interestingly indicates that this con-

sists of densely packed nanoparticles with particle size in the range of 20–50 nm (a few are marked as yellow circles). This suggests that distinct ZnO, SnO_2 and Zn_2SnO_4 nanoparticles got assembled closely in a definite pattern to form each single fiber having an overall diameter varying in the range of 700 nm to 2 μm (Fig. 3a–c). For instance, the measured diameter of the representative fiber in Fig. 3c is 1.94 μm as depicted by a yellow dotted line. This proper microstructure of the composite fiber has been further substanti-ated by the TEM images exhibited in Fig. 3d and e. The HRTEM image in Fig. 3f effectively exhibits the existence of three types of lattice fringes corresponding to (100), (110) and (111) crystallographic plane of ZnO, SnO_2 and Zn_2SnO_4, respectively. Inset exhibits the corresponding FFT of the HRTEM. Moreover, the SAED pattern in Fig. S1(a) indicates the (002), (110) and (112) planes of ZnO, (111), (110) and (211) planes of SnO_2 and (311) plane of Zn_2SnO_4. This observation further confirms the existence of all the three semi-conducting oxide nanoparticles in a single composite fiber. A more uniform distribution was observed for the phase pure Zn_2SnO_4 fibers formed at the elevated calcination temperature of 1000 °C (Fig. 4a). Interestingly, the fibers became randomly porous through-out the length along with hollow nature in certain areas (Fig. 4b) at this particular processing condition. The thickness of the hollow fibers also varied throughout the length of the fiber. For example, the measured thicknesses are 185, 379 and 715 nm, respectively, in three different areas marked as 1, 2, 3, respectively, as exhib-ited in the inset of Fig. 4b. The high resolution FESEM image in Fig. 4c exhibits the characteristics of a single fiber having diam-eter of around 1.19 nm formed by the assimilation of the phase pure Zn_2SnO_4 particles with particle size varying in the range of 60–350 nm. It is worth noting that at higher temperature the indi-vidual binary oxides nanoparticles of ZnO and SnO_2 reacted to form comparatively larger sized and more stable ternary oxide Zn_2SnO_4 leading to the creation of several interparticle pores throughout the structure resulting in the formation of porous fibers. The presence of internal pores within the fiber has further been established by the TEM images shown in Fig. 4d and e. The HRTEM image in Fig. 4f reveals the lattice fringes which corresponds exclusively to the (111) crystallographic plane of Zn_2SnO_4 with a d-spacing of 4.97 Å finally confirming the phase purity and crystallinity of the formed fiber at this temperature. The FFT of the corresponding HRTEM also supports this conclusion. Random distribution of the pores is also evident from the HRTEM shown in Fig. 4f. In addition the SAED pattern shown in Fig. S1 (b) exclusively corresponds to the (220), (311), (400), (422) and (440) planes of Zn_2SnO_4 only. The porous and hollow nature of the fibers makes them more useful for better adsorption of the dye molecules. This indubitably offers a preferable platform for immediate interaction of the dye molecules with the fibers acting as photoanode and photocatalyst in two diverse appli-cations. The calcination temperature dependent phase transition has further been verified by the IR and Raman spectroscopy. The broad IR active band cantered at $\sim 3425 \, cm^{-1}$ for all the samples in Fig. 5A can be assigned to the stretching vibration of the OH bonds of the adsorbed water. The intensity of the peak decreased gradually with increase in the calcination temperature from 700 to 1000 °C and has been depicted in Fig. 5A. Fig. 5A (inset) evidently exhibited the predominant band at $571 \, cm^{-1}$ for the fiber calcined at 1000 °C. This assigns to the characteristic vibration band for Sn-O-Zn bond of the spinel Zn_2SnO_4 fiber formed at this particular condition [28–30]. On the contrary, the appearance of the bands at 525, 420 and $656 \, cm^{-1}$, respectively, for Zn-O and Sn-O vibrations of ZnO and SnO_2 along with Zn_2SnO_4 in the form of weak band at $571 \, cm^{-1}$ evidences the formation of ZnO-SnO_2-Zn_2SnO_4 composite fiber at 700 °C and 800 °C and corroborates the results observed from the XRD experiments. The intense Raman active band at $669 \, cm^{-1}$ of A_1g symmetry corresponds to the typical Raman shift of Zn_2SnO_4 originated due to the symmetric stretching of the Zn-O bonds in the
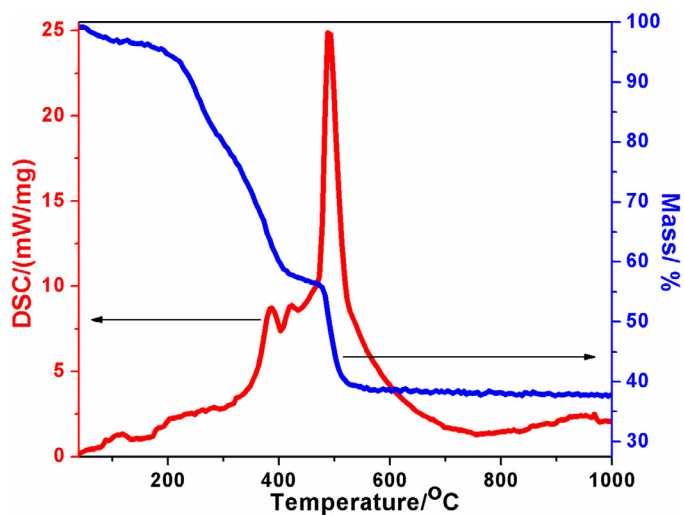
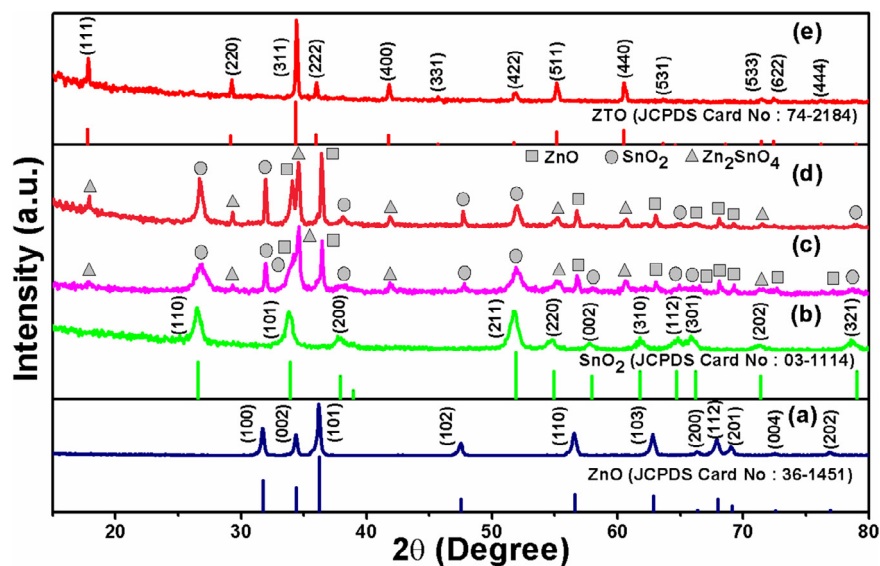**Fig. 1.** TG-DSC plots of the as formed electrospun fiber.

Fig. 2. The X-ray diffraction pattern of (a) ZnO, (b) SnO_2, as prepared fiber calcined at (c) 700, (d) 800 and (e) 1000 °C, respectively.
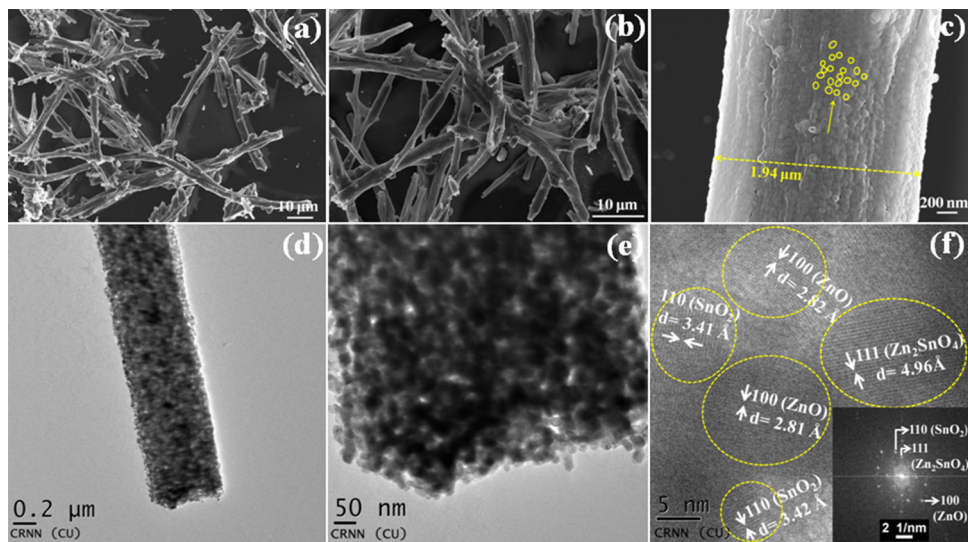

Fig. 3. (a), (b), (c) FESEM images of the composite fiber with increasing magnification, (d), (e) TEM images of a single fiber, (f) HRTEM image of the same, inset exhibits the corresponding FFT.
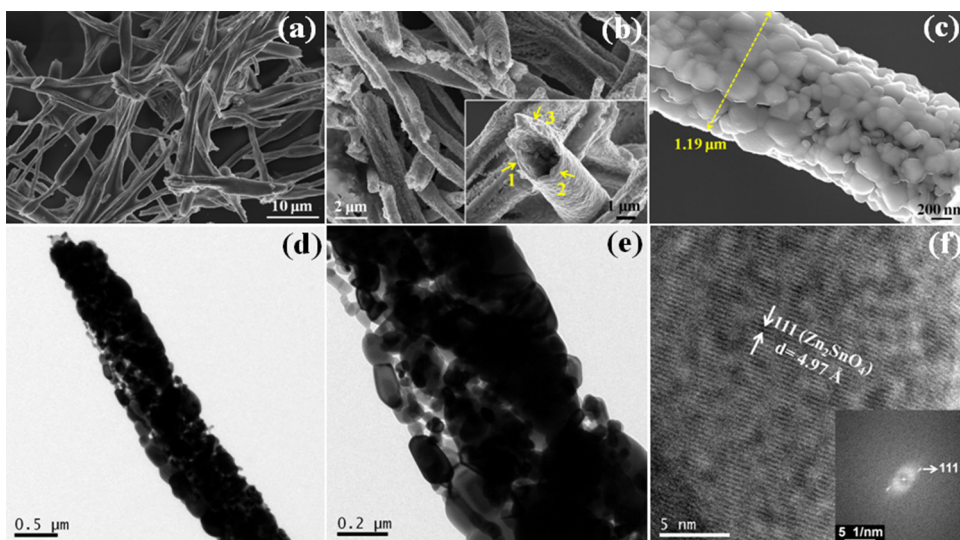
Fig. 4. (a), (b), (c) FESEM images of the phase pure Zn_2SnO_4 fiber with increasing magnification, inset of (b) exhibits the hollow fiber, (d), (e) TEM images of a single fiber, (f) HRTEM image of the same, inset shows the corresponding FFT.
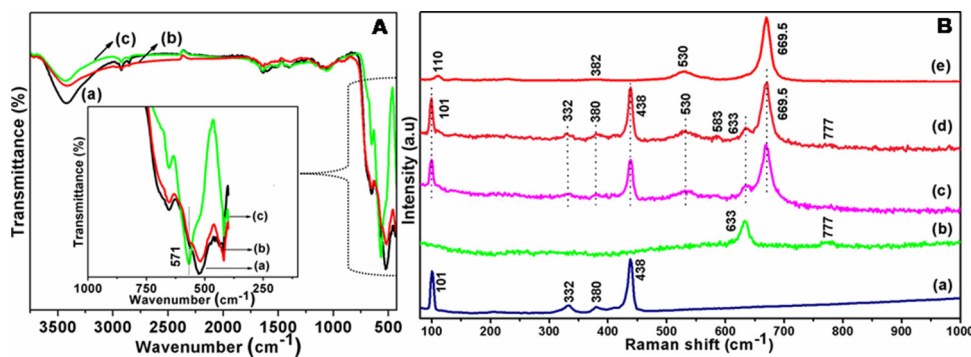

Fig. 5. A. FTIR spectra of the as prepared fiber calcined at (a) 700, (b) 800 and (c) 1000 °C, B. Raman spectra of (a) ZnO, (b) SnO_2, the as prepared fiber calcined at (a) 700, (b) 800 and (c) 1000 °C, respectively.

ZnO_4 tetrahedra of the inverse spinel Zn_2SnO_4 fiber (Fig. 5B). The other phonon modes of the particular fiber appeared at 530 cm^{-1} and 382 cm^{-1} which, respectively, correspond to the symmetric F2g(1) and asymmetric F2g(2) bending of oxygen atoms of the M-O bonds of the MO_6 octahedra (M = Zn or Sn) (Fig. 5B-e). This ascertains the formation of the phase pure Zn_2SnO_4 fiber [28,29,31]. Moreover, the Raman active band at 626 cm^{-1} corresponding to the presence of defects in Zn_2SnO_4 is also lacking here [31]. The fiber calcined at 800 °C (Fig. 5B-d) exhibited the characteristic Raman scattering peaks for hexagonal Wurtzite phase of ZnO at 438, 101, 380 and 332 cm^{-1} attributed to E_2 High, E_2 Low and A_1 (TO) modes and multiphonon scattering process, respectively. Moreover, the characteristic Raman scattering peaks for tetragonal SnO_2 phase have also been observed at 633 and 777 cm^{-1} corresponding to the A_1g and B_2g vibration modes, respectively. In addition, the presence of Raman active modes of Zn_2SnO_4 also confirms the formation of a ZnO-SnO_2-Zn_2SnO_4 composite fiber at 800 °C and corroborates the previous inferences. It is worth mentioning the significant Raman active mode of the composite fiber at 583 cm^{-1} attributed to the E_1 (LO) mode appears exclusively from the oxygen vacancy defects of ZnO [10]. Therefore, it can be inferred that in the ZnO-SnO_2-Zn_2SnO_4 composite, the ZnO is the preferred component to exhibit oxygen vacancy [10]. The composition of ZnO: SnO_2: Zn_2SnO_4 varied in different proportion for the fiber calcined at further lower temperature, for example the spectra of 700 °C calcined sample have been exhibited in Fig. 5B-c. The Raman active

modes of the ZnO and SnO_2 have also been displayed for comparison of the phases in Fig. 5B-a and b, respectively. The valence states of the fundamental elements Zn, Sn and O of the Zn_2SnO_4 fiber along with the ZnO-SnO_2-Zn_2SnO_4 composite have been identified through X-ray photoelectron spectroscopy (XPS) measurements (Fig. 6). The survey scan of XPS spectra of both the samples in Fig. 6(a) exhibited a couple of well-defined peaks at 494.7 eV and 486.3 eV originating due to the spin orbit coupling of 3d electrons corresponding to the binding energies of Sn $3d_{3/2}$ and Sn $5d_{5/2}$, respectively [32,33]. These peaks are considered as characteristics of Sn^{4+} present both in Zn_2SnO_4 lattice and ZnO-SnO_2-Zn_2SnO_4 composite. In addition, the spectra for Zn 2p in Fig. 6(b) centered at around 1044.4 eV and 1021.4 eV can be attributed to the spin orbit split peaks of Zn $2p_{1/2}$ and Zn $2p_{3/2}$, respectively, corresponding to Zn^{2+} cations in both the lattices. No significant dissimilarity in spectral shape and binding energy positions of the spectra of Sn 3d and Zn 2p for both indicates any major difference in the electronic structures of Zn and Sn in the single phase Zn_2SnO_4 and in the multi phase ZnO-SnO_2-Zn_2SnO_4 fiber. The highly symmetric peak at 530.1 eV can be assigned to the binding energy of O 1s of Zn_2SnO_4 (Fig. 6c). This dominant and symmetric nature of the spectra has been considered as characteristics of O^{2-} ions in the Zn-O-Sn metal oxide lattice framework. The XPS data ascertains that all the three basic elements Zn, Sn and O possesses only the appropriate as well as most stable valence state of +II, +IV and −II, respectively, to form the cubic spinel Zn_2SnO_4. Thus, the successful formation
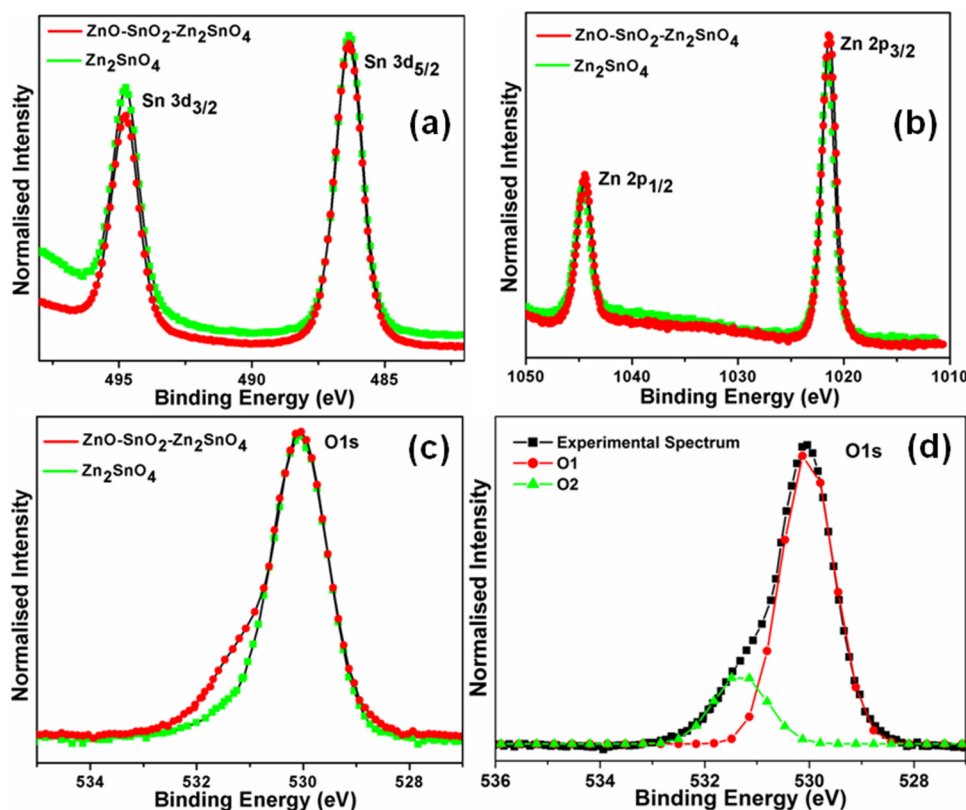
Fig. 6. XPS spectra of spin-orbit split peaks of (a) Sn 3d, (b) Zn 2p and (c) O 1s, respectively, of single phase Zn_2SnO_4 and ZnO-SnO_2-Zn_2SnO_4 composite fiber, (d) spectral decomposition of the O 1 s spectra of ZnO-SnO_2-Zn_2SnO_4 composite fiber results two differen type of oxygen environment, depicts as O1 and O2.
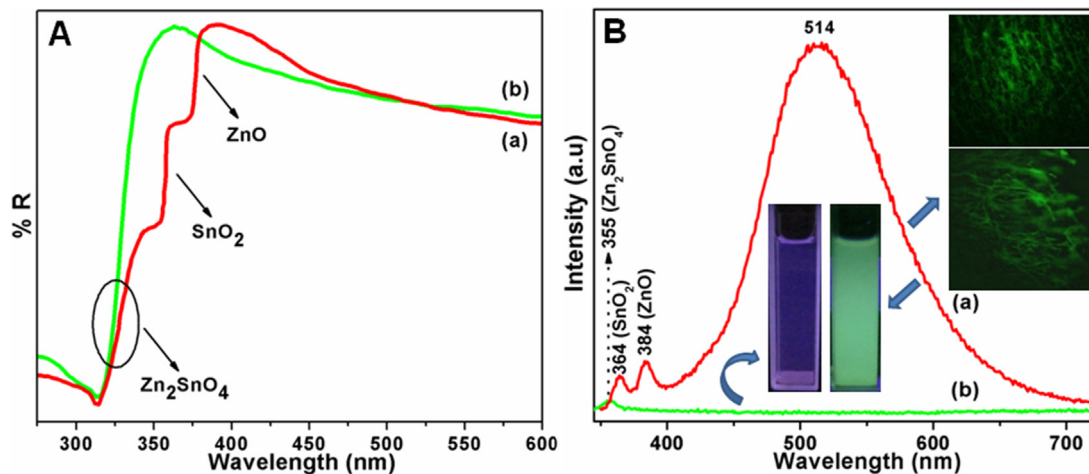

Fig. 7. A. DR spectra of (a) ZnO-SnO_2-Zn_2SnO_4 composite and (b) phase pure Zn_2SnO_4 fibers, B. Room temperature emission spectra of (a) ZnO-SnO_2-Zn_2SnO_4 composite and (b) phase pure Zn_2SnO_4 fibers. Inset shows the fluorescence microscopic images of the composite fiber.

of phase pure Zn_2SnO_4 fiber at the higher calcination temperature of 1000 °C has been confirmed from XPS data as well. On the contrary, a notable asymmetric spectrum appeared for the O 1s of ZnO-SnO_2-Zn_2SnO_4 (Fig. 6c). On deconvolution, the asymmetric O 1s spectrum split into two components exhibiting peak maximum at 530.1 eV (O1 component) and 531.4 eV (O2 component) as depicted in Fig. 6d. The dominant O1 component is characteristics of O^{2-} ions in the Zn-O-Sn metal oxide lattice framework as it is common to the pure Zn_2SnO_4 fiber whereas the O2 component at higher binding side originates due to the presence of oxygen vacancy defects in the ZnO matrix of ZnO-SnO_2-Zn_2SnO_4 lattice. Presence of oxygen defects in ZnO has been reported by us earlier

through XPS studies [10]. Therefore, along with the formation of the single phase Zn_2SnO_4 the oxygen vacancy defects also dissociate away upon calcining the ZnO-SnO_2-Zn_2SnO_4 at 1000 °C. The room temperature diffuse reflectance spectrum of the ZnO-SnO_2-Zn_2SnO_4 composite and phase pure and Zn_2SnO_4 fiber have been performed and are respectively displayed in Fig. 7A-a and b. The sharp decrease in% R around 350 nm in Fig. 7A-a signifies the interband electronic absorption of the Zn_2SnO_4 fiber with an estimated band gap (E_g) of 3.7 eV from the Tauc's plot (not shown in Fig.). Three consecutive variations in the reflectance spectra of the composite fiber in Fig. 7A-b have been attributed to the existence of different phases. The estimated band gap decreased to 3.2-3.3 eV
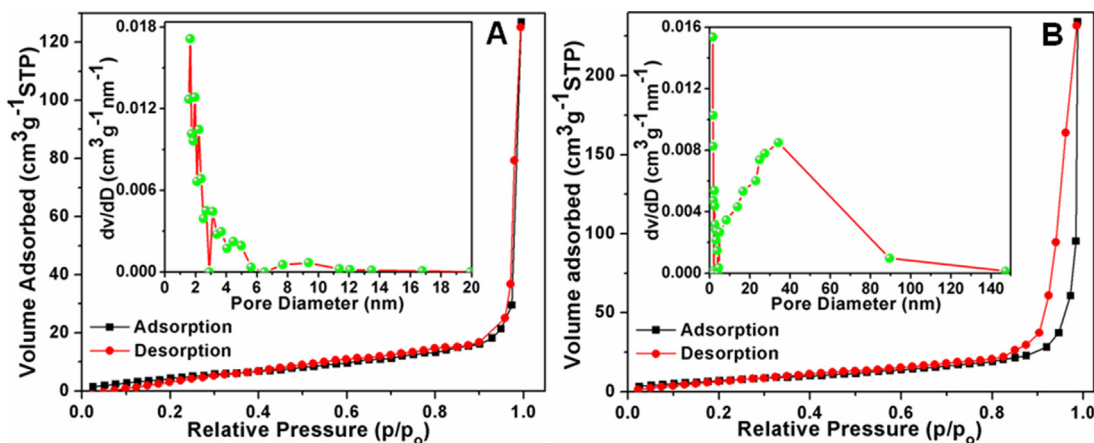
Fig. 8. A-B. N_2 adsorption-desorption isotherms of ZnO-SnO_2-Zn_2SnO_4 composite and phase pure Zn_2SnO_4 fibers, respectively. Insets exhibit their corresponding pore size distriutions.

which reflects the contribution of ZnO whereas the same for SnO_2 appeared around 3.4-3.5 eV. The room temperature photoluminescence (PL) spectrum of the composite fiber also exhibited multiple intra-band emissions (Fig. 7B-a). The band centered at 384 nm originates from the band edge emission (NBE) of ZnO. In addition, the broader one centered at 364 nm is considered to be an overlap of the band emissions of the remaining compositions predominantly SnO_2. The visible emission is absent in the phase pure fiber excluding a depressed peak at 355 nm for the band edge emission of Zn_2SnO_4 (Fig. 7B-b). The most important feature of the composite fiber in Fig. 7B-a is the exposition of an extraordinary intense visible emission in the green region with a λ_{max} of 514 nm originating exclusively from the single ionised oxygen vacancy defects of ZnO [10]. Inset of Fig. 7B exhibits the digital image of the green emission of the ethanolic dispersion of the composite fiber obtained by exciting under UV lamp (8W, 365 nm). In addition, the microscopic fluorescence images of the direct fiber also furnish excellent green emission which confirms the presence of surface defects in the ZnO-SnO_2-Zn_2SnO_4 composite. Interestingly, as anticipated the digital image of defect free phase pure Zn_2SnO_4 fiber was devoid of visible emission. The effect of native defects on the structural and optical properties of the semiconducting oxide materials has been demonstrated through various examples [10,34]. The obvious demarcation in surface area and porosity of the fiber samples were further ensured from the N_2 adsorption-desorption isotherms and BJH pore size distribution curves (Insets) in Fig. 8A-B. The typical type III isotherm of the dense fiber (Fig. 8A) successfully converted to mesoporous one exhibiting characteristic type IV isotherm with a loop for the relative pressure p/p_0 in the range of 0.82-1. Consequently, the average pore diameter improved to 32 nm for the phase pure Zn_2SnO_4 fiber (Fig. 8B inset) which was insignificant indeed in case of ZnO-SnO_2-Zn_2SnO_4 composite fiber (Fig. 8A inset) as obtained by the BJH method and corroborates the FESEM and TEM results. The BET analysis further revealed a higher surface area of 37.67 m^2/g for the uniform Zn_2SnO_4 fiber compared to ZnO-SnO_2-Zn_2SnO_4 composite having a surface area of 21.76 m^2/g. The observed structural, micro-structural, optical and physical characteristics of the fibers are crucial towards the applications of such materials in DSSCs and photocatalytic activity.

4. Device performance of the materials

The J-V characteristics of the cell fabricated with two different types of fibers consist of ZnO-SnO_2-Zn_2SnO_4 composite and pure Zn_2SnO_4 as photoanode are presented in Fig. 9A. The corresponding photovoltaic performances of the fabricated devices are summa-

Table 1
Photovoltaic properties of the ZnO-SnO_2-Zn_2SnO_4 composite and phase pure Zn_2SnO_4 fibers.

Fiber composition	Voc (V)	Jsc (mA/cm^2)	FF (%)	η(%) $\pm$ 0.01
ZnO-SnO_2-Zn_2SnO_4	0.70	3.81	42.54	1.17
Zn_2SnO_4	0.76	4.20	59.78	1.93

rized in Table 1. The phase pure Zn_2SnO_4 fiber exhibited a relatively higher open circuit voltage (Voc) and fill factor (FF) of 0.76 V and 59.78%, respectively, compared to the ZnO-SnO_2-Zn_2SnO_4 composite fiber which exhibited a lower Voc of 0.70 V and FF of 42.54%. At the same time the single phase hollow Zn_2SnO_4 fiber having several interparticle pores and larger surface area with a higher N719 dye loading capacity as confirmed from Fig. S2A was successful in generating a better short circuit current (Jsc) of 4.2 mA/cm^2 compared to composite fiber (3.8 mA/cm^2). The dye loading capacity is extremely crucial and important for a photoanode material to exhibit better performance in a DSSC device. Ultimately, a conversion efficiency of 1.93% have been achieved for the phase pure Zn_2SnO_4 fiber and that of only 1.17% have been obtained for the device fabricated with ZnO-SnO_2-Zn_2SnO_4 composite fiber. To the best of our knowledge, the conversion efficiency of 1.93% achieved using the synthesised phase pure Zn_2SnO_4 fiber as photoanode is the highest reported values for this type of fiber microstructure (Table S1) [35]. It is anticipated that due to the presence of three different oxides, the composite fiber introduce three successive energy levels corresponding to ZnO, SnO_2 and Zn_2SnO_4 just below the LUMO of the dye N719. The sensitizer which absorbs sunlight consisting of mostly visible radiation injects electron to the conduction band of the photoanode where it has to exceed all the individual energy level of the semiconducting oxides of the composite gradually according to their decreasing order of energy level before it gets released to the conducting substate. This retards the forward flow of photoelectron and an eventual possibility of recombination reactions increases from three simultaneous energy levels of three discrete phases of the composite fiber. On the other hand, in the fiber consisting of purely single phase Zn_2SnO_4 such a possibility of recombination is negligible. The corresponding energy level diagram of the DSSC fabricated with the composite semiconducting oxide as photoanode have been illustrated in Fig. 9B. The probable steps of recombination (R_1 and R_2) are marked red.

5. Photocatalytic activity

In order to further explore the utility of such fibers as photocatalysts for the degradation of organic pollutants in water, two
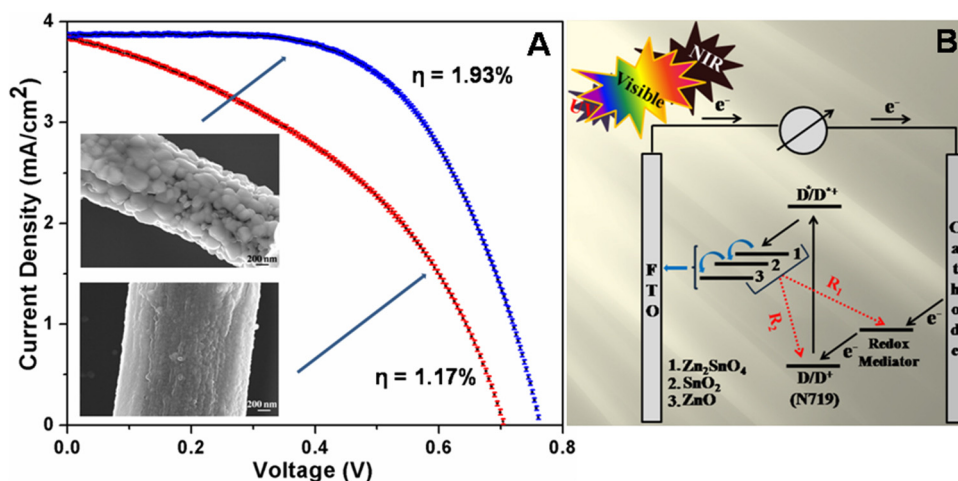
Fig. 9. A. J-V characteristics of ZnO-SnO$_2$-Zn$_2$SnO$_4$ composite (red) and phase pure Zn$_2$SnO$_4$ fiber (blue). B. Schematic illustration of the energy level diagram of a DSSC fabricated with the ZnO-SnO$_2$-Zn$_2$SnO$_4$ composite used as photoanode and the electron transfer pathways. (For interpretation of the references to colour in this figure legend, the reader is referred to the web version of this article.)
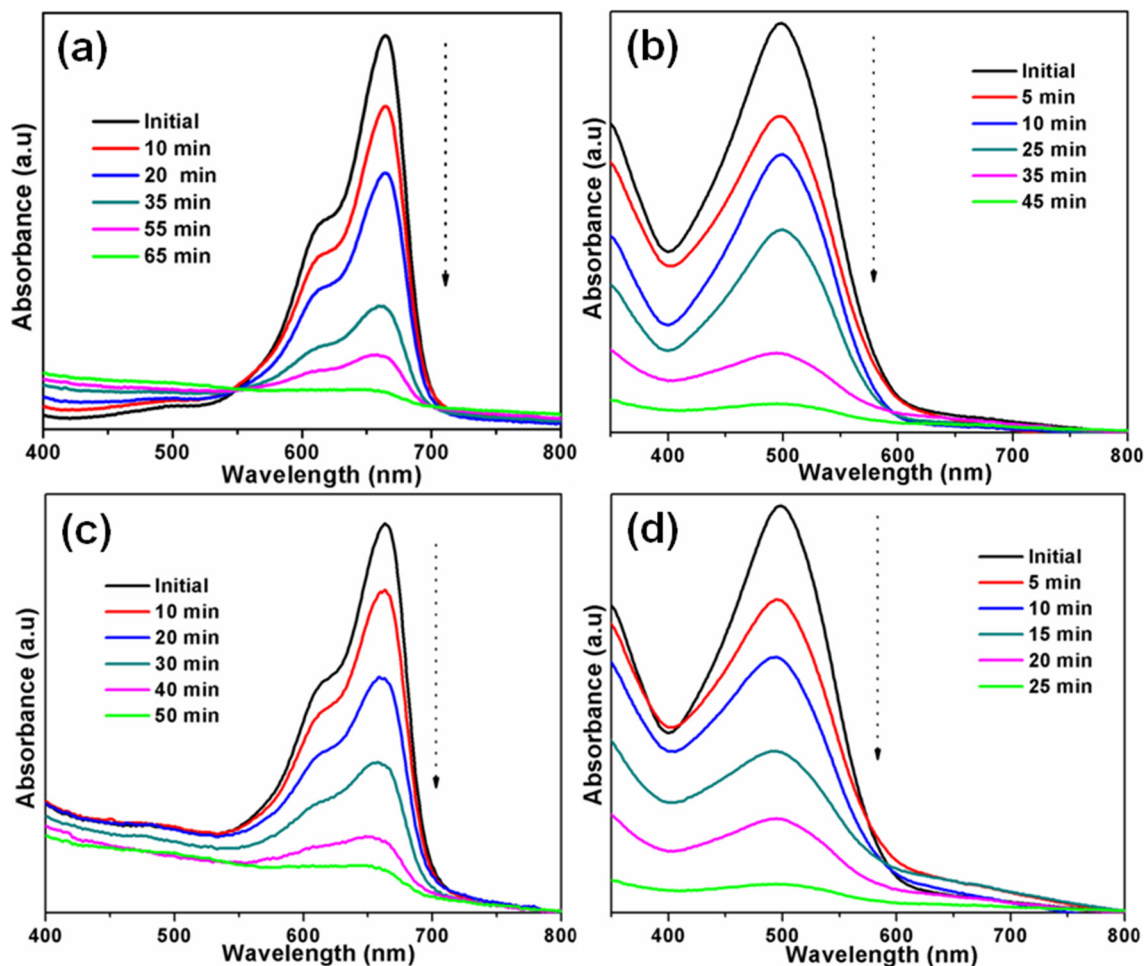

Fig. 10. Absorption spectra of (a) and (c) Methylene Blue, (b) and (d) Congo Red in presence of the phase pure Zn$_2$SnO$_4$ and ZnO-SnO$_2$-Zn$_2$SnO$_4$ composite fiber, respectively, at different time intervals of UV irradiation.

different types of dyes namely a cationic dye Methelene Blue (MB) and dye anionic Congo Red (CR) were selected for our initial experiments. The respective absorption maximum at 664 nm of MB and 497 nm of CR were explicitly monitored during the controlled degradation experiments presented here (Fig. 10a–d). The chemical structures of MB and CR along with the digital images of

dye solutions in presence of ZnO-SnO$_2$-Zn$_2$SnO$_4$ composite fiber at different UV illumination times are depicted in Fig. S3. Fig. 11A and B indubitably revealed that a minimum of around 100 mg samples were sufficient for the degradation of around 10^{-5} mol of dye molecules. Careful monitoring of the degradation kinetics in dark once again ascertains the porous Zn$_2$SnO$_4$ fiber having a
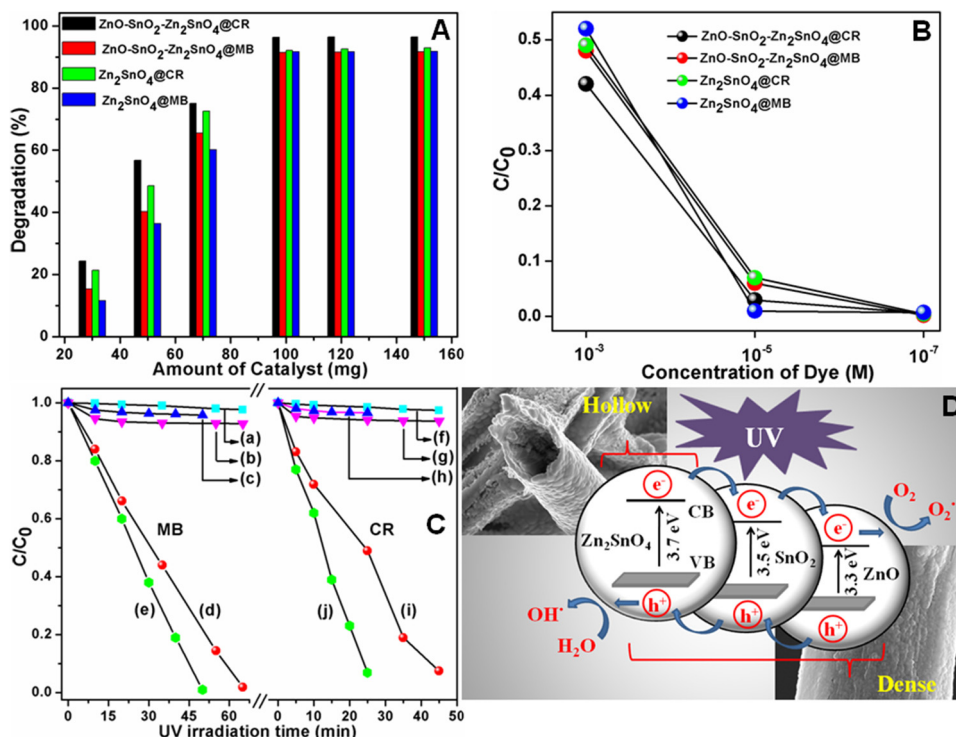
Fig. 11. A. Degradation efficiencies of 10^{-5} (M) dyes as a function of the amount of fiber samples. B. Photodegradations of the dyes of concentrations 10^{-3}, 10^{-5} and 10^{-7} (M) in presence of 100 mg catalysts. C. The comparative photodegradation profile of Methylene Blue (a) in absence of catalyst, (b) and (c) in presence of the phase pure Zn_2SnO_4 and $ZnO-SnO_2-Zn_2SnO_4$ composite fiber, respectively, in dark, (d) and (e) represent the same at different UV irradiation durations. Congo Red (f) in absence of catalyst, (g) and (h) in presence of the phase pure Zn_2SnO_4 and $ZnO-SnO_2-Zn_2SnO_4$ composite fiber, respectively, in dark, (i) and (j) represent the same at different UV irradiation durations. D. Schematic illustration of the energy band structure diagram and the electron-hole pair separation pathway in the composite fiber.
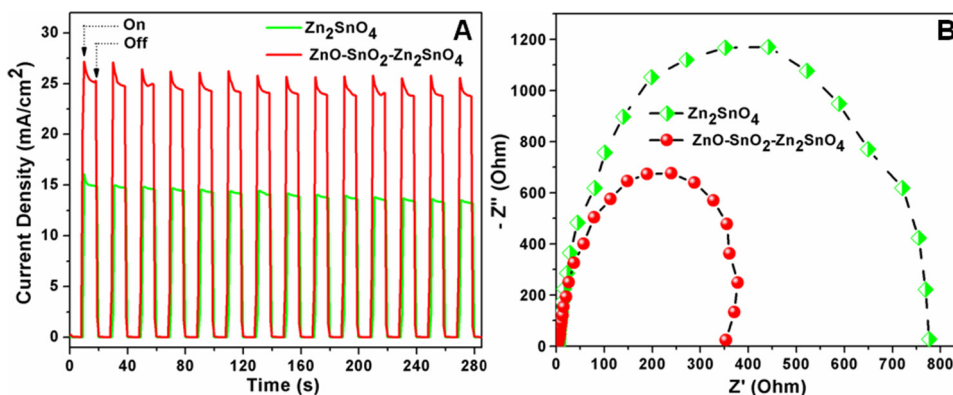

Fig. 12. A Transient photocurrent response for the phase pure Zn_2SnO_4 and $ZnO-SnO_2-Zn_2SnO_4$ composite fiber. B. Electrochemical impedance spectra of the same.

higher surface area as a superior adsorber of MB and CR similar to N719 (Fig. S2B). Interestingly, the photo-degradation performance of the samples has been compared to the photovoltaic performance where the $ZnO-SnO_2-Zn_2SnO_4$ composite fiber exhibited a better photocatalytic activity than the phase pure Zn_2SnO_4 fiber towards both MB and CR (Fig. 11C). Pure Zn_2SnO_4 fiber possess the optical absorption (E_g 3.7 eV) absolutely in the UV region. Under UV irradiation the possibility of severe recombination reaction between the photo-generated electrons and holes which impede the photocatalytic efficiency of the same. The formed heterojunction among Zn_2SnO_4 with other UV active semiconducting oxides SnO_2 (E_g 3.5 eV) and ZnO (E_g 3.3 eV) having relatively low lying conduction bands could favour the electron transfer from Zn_2SnO_4 to SnO_2 and further to ZnO where SnO_2 and ZnO acts as the sink. Moreover, the extensive oxygen vacancy defects in the $ZnO-SnO_2-Zn_2SnO_4$ composite fiber as revealed from the Raman, XPS and PL

spectra in Fig. 5B(d), 6(d) and 7B(a), respectively, could also be able to trap the photo electrons generated upon UV irradiation temporarily [9]. Such characteristics of the composite fiber could profoundly increase the electron-hole separation, eventually suppress the recombination and enhances the charge transfer process. The energy band structure diagram along with the electron-hole pair separation pathway in the composite fiber is schematically represented in Fig. 11D. The separation efficiency of the photo-generated charge carriers of both the composite and phase pure fiber were investigated by transient photocurrent responses of the same for several cycles with an on-off pulse duration of 10 s. The negligible photocurrent response in dark repeatedly enhanced to a considerable extent immediately upon UV illumination for all the cycles as observed from Fig. 12A. The higher photocurrent density of the $ZnO-SnO_2-Zn_2SnO_4$ composite fiber compared to phase pure Zn_2SnO_4 confirms the feasibility of more efficient separation
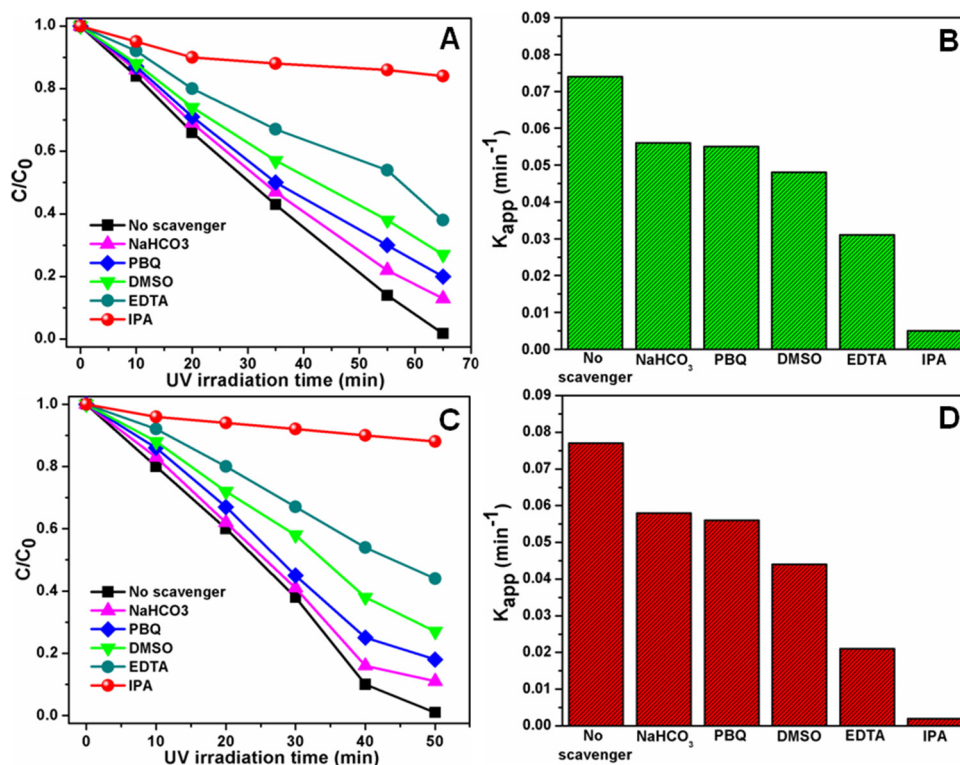
Fig. 13. A and C. Photocatalytic degradation performance of phase pure Zn_2SnO_4 and ZnO-SnO_2-Zn_2SnO_4 composite fiber, respectively, towards Methylene Blue in presence of different scavengers under UV illumination, B and D. Effect of different scavengers on the degradation of MB by phase pure Zn_2SnO_4 and ZnO-SnO_2-Zn_2SnO_4 composite fiber, respectively.
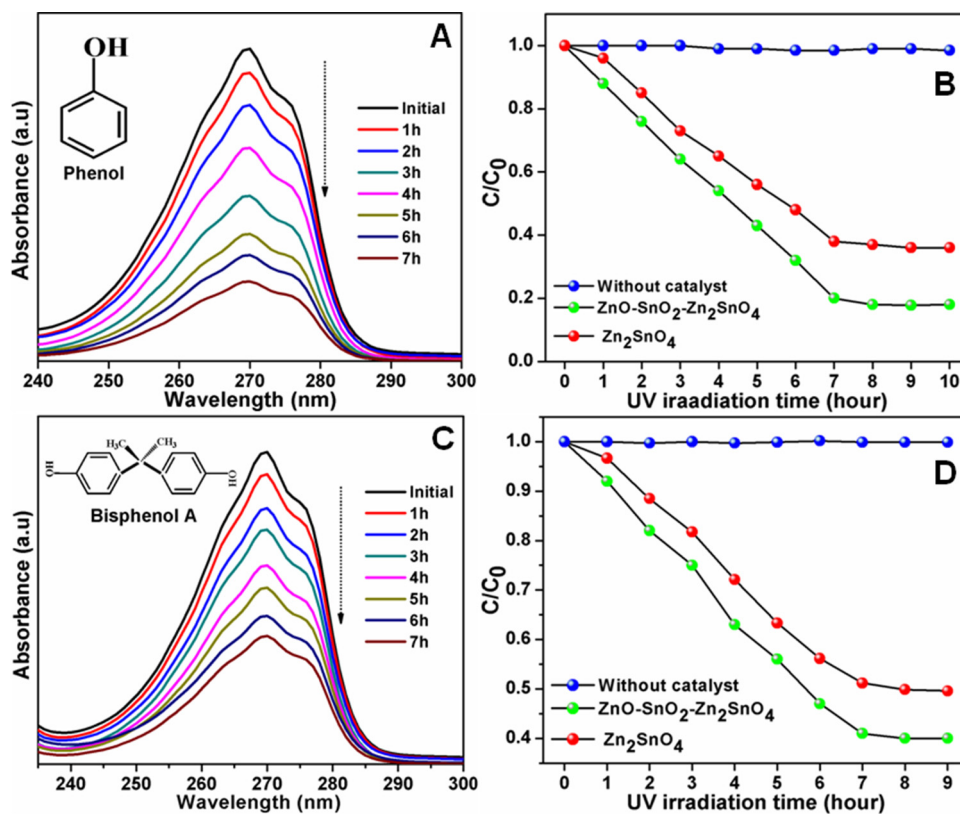

Fig. 14. A and C. Absorption spectra of Phenol and Bisphenol A, respectively, in presence of the ZnO-SnO_2-Zn_2SnO_4 composite fiber at different time intervals of UV irradiation. B and D. The comparative photodegradation profile of Phenol and Bisphenol A, respectively, in presence of the phase pure Zn_2SnO_4 and ZnO-SnO_2-Zn_2SnO_4 composite fiber, respectively, under different UV irradiation durations.

of photogenerated electrons and holes for this particular photocatalyst (Fig. 12A) [21,23,25]. Moreover, the lower resistance of the composite as revealed from the semicircle in the Nyquist plot in Fig. 12B in the manuscript further affirms the previous inferences in favour of the ZnO-SnO$_2$-Zn$_2$SnO$_4$ composite fiber regarding the accelerated charge transfer process [21,23,26]. The separated electrons and holes are essential indeed in generating active radical species during photocatalytic reaction. The photogenerated holes are being trapped by the hydroxyl group or H$_2$O molecules at the surface of the catalyst producing OH$^•$ radicals. The electrons elsewhere react with the dissolved oxygen molecules and generate the same OH$^•$ radicals following a multistep reaction. The (OH$^•$) radicals are mainly accounted for the photo oxidation of the organic dye molecules [18]. Considering all the conventional reactive species during a photochemical reaction, the major and active OH$^.$ (hydroxyl) radical behind the photo-degradation activities of both fibers have been isolated by systematic quenching experiments with MB using specific scavengers namely NaHCO$_3$ (as absorbed OH$^•$ quencher), DMSO (as e$^-$ quencher), para benzoquinone (PBQ, as O$_2^{.-}$ quencher), EDTA (as hole trapping agent) and isopropylalcohol (IPA, as OH$^.$ quencher) [23]. Fig. 13A,C manifest an immense suppression in photodegradation in presence of IPA in particular followed by EDTA to some extent for both the fibers whereas the performance of other scavengers were almost insignificant. The photo-degradation kinetics in presence of quenchers follow the first order simplified Langmuir-Hinshelwood kinetic model. The apparent first order rate constant (K$_{app}$) was determined from the equation, $\ln(C_0/C) = K_{app}t$, where K$_{app}$ implies the gradient of the respective $\ln(C_0/C)$ vs time (t) plot. The collection of all the obtained K$_{app}$ values in Fig. 13 B,D again substantiates the utmost effect of the scavenger IPA in reducing the photodegradation rates to a significant manner confirming the inevitable effect of the (OH$^•$) radicals for both fibers in common [21,23]. Briefly, the lesser recombination of the photogenerated electron and holes in the ZnO-SnO$_2$-Zn$_2$SnO$_4$ composite fiber leads to the formation of more active (OH$^.$) radicals only making it a preferable photocatalyst than the phase pure Zn$_2$SnO$_4$ fiber. However, the overall photocatalytic performances of the prepared samples are quite considerable among the reported performances of such kinds of systems as summarised in Table S2 [36–45]. It is worth mentioning that both the composite and phase pure fiber exhibited no significant loss in photocatalytic efficiency even after recycling the catalyst for six times which highlights the effective reusability of the sample as an effective photocatalyst (Fig. S2C). Moreover, the representative FESEM image of the relatively efficient ZnO-SnO$_2$-Zn$_2$SnO$_4$ composite fiber after six successive cycles towards degradation of MB in Fig. S2D elucidates that the microstructure also remained more or less unaffected after the photocatalytic tests. This further supports in favour of the endurance of the fiber morphologies of the prepared samples. The photocatalytic activities of the two different fibers were eventually assessed for the degradation of the non-absorbing organic pollutants such as Phenol and Bisphenol A (Fig. 14A,C). After an assessment of 7 h, the ZnO-SnO$_2$-Zn$_2$SnO$_4$ composite fiber was successful in degrading a considerable percentage of Phenol (78%) and Bisphenol A (61%). On the contrary, the phase pure porous Zn$_2$SnO$_4$ fiber was only able to degrade 64% and 49% of Phenol and Bisphenol A, respectively (Fig. 14B,D). This again supports in favour of the ZnO-SnO$_2$-Zn$_2$SnO$_4$ composite fiber, as a better photocatalyst than the hollow and porous Zn$_2$SnO$_4$ fiber in spite of it being a better dye adsorber as demonstrated through various experiments (Fig 14).

6. Conclusions

In summary, the ZnO-SnO$_2$-Zn$_2$SnO$_4$ composite fiber and phase pure Zn$_2$SnO$_4$ fiber were synthesized by calcining the as prepared electrospun fiber at 800 and 1000 °C, respectively. A single composite oxide fiber consisting of a dense assembly of the ZnO, SnO$_2$ and Zn$_2$SnO$_4$ nanoparticles were formed initially. The individual binary oxides ZnO and SnO$_2$ nanoparticles diffusing at an elevated temperature of 1000 °C resulted in the formation of phase pure ternary oxide Zn$_2$SnO$_4$ nanoparticles by simultaneous creation of several inter particle pores throughout the nanoparticles assembly. Emission and fluorescence microscopic image display an interesting green emission of the composite fiber owing to the surface oxygen vacancy defects present in ZnO. Through various spectroscopic and microscopic techniques it was confirmed that the dense and fluorescent ZnO-SnO$_2$-Zn$_2$SnO$_4$ composite fiber practically converted into a non fluorescent but porous phase pure Zn$_2$SnO$_4$ fiber at higher calcination temperature. The DSSC device fabricated with the single phase, porous and hollow Zn$_2$SnO$_4$ fiber as photoanode got facilitated due to the favourable single step photoelectron transport and higher dye loading. As a consequence, this exhibited A relatively improved Voc of 0.76 V, FF of 59.78% and Jsc of 4.2 mA/cm^2 whereas a depressed Voc of 0.70 V, FF of 42.54% and Jsc of 3.8 mA/cm^2 had been achieved for the dense composite fiber. The maximum conversion efficiency of 1.93% have been achieved for the pure Zn$_2$SnO$_4$ porous fiber with N719 dye which is even higher than the only reported efficiency of 1.41% for the amorphous Zn$_2$SnO$_4$ nanofibers. On the contrary, the composite fiber having a heterojunction of ZnO-SnO$_2$-Zn$_2$SnO$_4$ exhibited superior electron-hole separation phenomenon followed by suppressed recombination upon UV irradiation resulting in the generation of more active OH$^•$ radicals during photocatytic reactions. This is the decisive characteristics of the composite in establishing the same as a better performer towards the photo degradation of the textile dyes MB and CR and non-absorbing organic pollutants such as Phenol and Bisphenol A.

Notes

The authors declare no competing financial interest.

References

[1] Y.N. Xia, P.D. Yang, Y.G. Sun, Y.Y. Wu, B. Mayers, B. Gates, Y.D. Yin, F. Kim, Y.Q. Yan, Adv. Mater. 15 (2003) 353–389.
[2] A.I. Hochbaum, R. Chen, R.D. Delgado, W. Liang, E.C. Garnett, M. Najarian, A. Majumdar, P. Yang, Nature 451 (2008) 163–167.
[3] J.R. Heath, Acc. Chem. Res. 41 (2008) 1609–1617.
[4] L.C. Palmer, S.I. Stupp, Acc. Chem. Res. 41 (2008) 1674–1684.
[5] J. Liu, C. Cheng, W. Zhou, H. Li, H.J. Fan, Chem. Commun. 47 (2011) 3436–3438.
[6] Y. Li, X. Fang, N. Koshizaki, T. Sasaki, L. Li, S. Gao, Y. Shimizu, Y. Bando, D. Golberg, Adv. Funct. Mater. 19 (2009) 2467–2473.
[7] Y. Li, T. Sasaki, T. Shimizu, N. Koshizaki, J. Am. Chem. Soc. 130 (2008) 14755–14762.
[8] G. Shen, P.C. Chen, K. Ryu, C. Zhou, J. Mater, Chemistry 19 (2009) 828–839.
[9] S. Mukhopadhyay, P.P. Das, S. Maity, P. Ghosh, P.S. Devi, Appl. Cat. B: Environ. 165 (2015) 128–138.
[10] P.P. Das, S.A. Agarkar, S. Mukhopadhyay, M. Unnikrishnan, S.B. Ogale, P.S. Devi, Inorg. Chem. 53 (2014) 3961–3972.

[11] V. Thavasi, G. Singh, S. Ramakrishna, Energy Environ. Sci. 1 (2008) 205–221.
[12] K. Mukherjee, T.H. Teng, R. Jose, S. Ramakrishna, Appl. Phys. Lett. 95 (2009) 012101–012103.
[13] I.D. Kim, J.M. Hong, B.H. Lee, D.Y. Kim, E.K. Jeon, D.K. Choi, D.J. Yang, Appl. Phys. Lett. 91 (2007), 163109–2.
[14] Q. Wali, A. Fakharuddin, I. Ahmed, H. Md, J. Ab Rahim, R. Ismail, J. Jose, Mater. Chem. A 2 (2014) 17427–17434.
[15] T. Cao, Y. Li, C. Wang, Z. Zhang, M. Zhang, C. Shao, Y. Liu, J. Mater. Chem. 21 (2011) 6922–6927.
[16] S. Zhan, D. Chen, X. Jiao, C. Tao, J. Phys. Chem. B 110 (2006) 11199–11204.
[17] Z. Li, Y. Zhou, W. Mao, Z. Zou, J. Power Sources 274 (2015) 575–581.
[18] Z. Zhang, C. Shao, X. Li, L. Zhang, H. Xue, C. Wang, Y. Liu, J. Phys. Chem. C 114 (2010) 7920–7925.
[19] Z. Zhang, C. Shao, X. Li, C. Wang, M. Zhang, Y. Liu, Appl. Mater. Interfaces 2 (2010) 2915–2923.
[20] X. Qian, D. Yue, Z. Tian, M. Reng, Y. Zhu, M. Kan, T. Zhang, Y. Zhao, Appl. Catal. B Environ. 193 (2016) 16–21.
[21] Y. Liang, S. Lin, Li Liu, J. Hu, W. Cui, Appl. Catal. B: Environ. 164 (2015) 192–203.
[22] L. Liu, L. Ding, W. An, S. Lin, J. Hu, Y. Liang, W. Cui, RSC Adv. 6 (2016) 29202–29209.
[23] W. Cui, W. An, L. Liu, J. Hu, Y. Liang, J.Hazard. Mater. 280 (2014) 417–427.
[24] Y. Zhua, Y. Wang, Q. Lingb, Y. Zhu, Appl. Catal. B: Environ. 200 (2017) 222–229.
[25] L. Liu, Y. Qi, J. Lu, S. Lin, W. An, Y. Liang, W. Cui, Appl. Catal. B Environ. 183 (2016) 133–141.
[26] W. Cui, H. Wanga, L. Liua, Y. Lianga, J.G. McEvoy, Appl. Surf. Sci. 283 (2013) 820–827.
[27] J. Wang, H. Li, S. Meng, L. Zhang, X. Fu, S. Chen, Appl. Catal. B: Environ. 200 (2017) 19–30.
[28] P.P. Das, P.S. Devi, Inorg. Chem. 53 (2014) 10797–10799.
[29] P.P. Das, A. Roy, S. Das, P.S. Devi, Phys. Chem. Chem. Phys. 18 (2016) 1429–1438.
[30] S. Mihaiu, I. Atkinson, O. Mocioiu, A. Toader, E. Tenea, M. Zaharescu, Rev. Roum. Chim. 56 (2011) 465–472.
[31] V. Sepelak, S.M. Becker, I. Bergmann, S. Indris, M. Scheuermann, A. Feldhoff, C. Kubel, M. Bruns, N. Sturzl, A.S. Ulrich, M. Ghafari, H. Hahn, C.P. Grey, K.D. Becker, P. Heitjans, J. Mater. Chem. 22 (2012) 3117–3126.
[32] Z. Li, Y. Zhou, J. Zhang, W. Tu, Q. Liu, T. Yu, Z. Zou, Cryst. Growth Des. 12 (2012) 1476–1481.
[33] Z. Chen, M. Cao, C. Hu, J. Phys. Chem. C. 115 (2011) 5522–5529.
[34] H. Kaftelen, K. Ocakoglu, R. Thomann, S. Tu, S. Weber, E. Eedem, Phys. Rev. B 86 (2012), 0141131-1-8.
[35] S.H. Choi, D. Hwang, D.Y. Kim, Y. Kervella, P. Maldivi, S.Y. Jang, R. Demadrille, I.D. Kim, Adv. Funct. Mater. 23 (2013) 3146–3155.
[36] L. Shi, Y. Dai, J. Mater. Chem. A 1 (2013) 12981–12986.
[37] S. Danwittayakul, M. Jaisai, J. Dutta, Appl. Catal. B: Environ. 163 (2015) 1–8.
[38] C. Liu, R. Roder, L. Zhang, Z. Ren, H. Chen, Z. Zhang, C. Ronning, Pu-Xian Gao, J. Mater. Chem. A 2 (2014) 4157–4167.
[39] M. Ben Ali, F. Barka-Bouaifel, H. Elhouichet, B. Sieber, A. Addad, L. Boussekey, M. Ferid, R. Boukherroub, J. Colloid. Interface. Sci. 457 (2015) 360–369.
[40] S. Danwittayakul, M. Jaisai, T. Koottatep, J. Dutta, Ind. Eng. Chem. Res. 52 (2013) 13629–13636.
[41] T.B. Ivetic, N.L. Fincur, Lj R. Dacanin, B.F. Abramovic, S.R. Lukic-Petrovic, Mater. Res. Bull. 62 (2015) 114–121.
[42] E.L. Foletto, S.L. Jahn, R.F.P. Muniz Moreira, J. Appl. Electrochem. 40 (2010) 59–63.
[43] E.L. Foletto, J.M. Simões, M.A. Mazutti, S.L. Jahn, E.I. Muller, L.S. Fagundes Pereira, E.M. Moraes Flores, Ceram. Int. 39 (2013) 4569–4574.
[44] M.N. Khan, M. Al-Hinai, A. Al-Hinai, J. Dutta, Ceram. Int. 40 (2014) 8743–8752.
[45] M.-J. Kim, S-Hun Park, Y.-D. Huh, Bull. Korean Chem. Soc. 32 (2011) 1757–1760.